A tin-based tandem electrocatalyst for CO_2 reduction to ethanol with 80% selectivity

Jie Ding
The Institute for Advanced Studies, Wuhan University,
Hongbin Yang
Southern University of Science and Technology
Xuelu Ma
Tsinghua University
Song Liu
Dalian Institute of Chemical Physics, Chinese Academy of Sciences
Wei Liu
Dalian Institute of Chemical Physics, Chinese Academy of Sciences https://orcid.org/0000-0002-4403-737X
Qing Mao
School of Chemical Engineering, Dalian University of Technology
Yanqiang Huang
Dalian Institute of Chemical Physics, Chinese Academy of Sciences
Jun Li
Tsinghua University https://orcid.org/0000-0002-8456-3980
Tao Zhang
Dalian Institute of Chemical Physics, Chinese Academy of Sciences https://orcid.org/0000-0001-9470-7215
Bin Liu (LIUBIN@ntu.edu.sg)
Nanyang Technological University https://orcid.org/0000-0002-4685-2052

Article

Keywords:

Posted Date: August 12th, 2022

DOI: https://doi.org/10.21203/rs.3.rs-1924605/v1

Additional Declarations: There is **NO** Competing Interest.

Version of Record: A version of this preprint was published at Nature Energy on October 30th, 2023. See the published version at https://doi.org/10.1038/s41560-023-01389-3.

Abstract

To date, only Cu-based catalysts have been used to generate appreciable C2 chemicals via the electrochemical CO_2 reduction reaction (CO_2RR). Here we report a Cu-free, Sn-based tandem electrocatalyst consisting of SnS_2 nanosheets and single Sn atoms coordinated with three oxygen atoms on three-dimensional (3D) carbon, which exhibits significant catalytic performance for selective reduction of CO_2 to ethanol with a maximum selectivity of approximately 82.5% at 0.9 V versus the reversible hydrogen electrode (RHE) and more than 70% over a wide electrode potential window from − 0.6 to -1.1 V versus RHE. This new catalyst maintains 97% of its initial activity (with a geometric current density of 17.8 $mA{\cdot}cm^{-2}$ at 0.9 V versus RHE) after 100 hours of reaction. First principles modeling shows that the dual active centers comprising Sn and O atoms that can respectively adsorb *CHO and *CO(OH) intermediates, therefore promoting C-C bond formation through an unprecedented *formyl-bicarbonate* coupling pathway.

Full Text

The use of electrochemical CO_2 reduction reaction (CO_2RR) to synthesize carbon-based fuels in conjunction with renewable electricity represents a promising strategy to address current concerns regarding global energy shortages and environmental issues such as climate change [1,2,3]. This process can potentially generate a wide variety of products [4,5,6,7,8], among which the liquid compounds are preferred [9] because of their high energy densities (e.g., -1366.8 kJ/mol for CH_3CH_2OH) and ease of storage when serving as substitutes for gasoline [10,11]. However, due to the high energy barrier to C-C bond formation, which competes with the formation of C-H or C-O bonds [12,13,14], the generation of multi-carbon liquid products via the CO_2RR is still very difficult. To date, Cu is the only electrocatalyst found able to generate C_n ($n \geq 2$) liquid products from the CO_2RR with appreciable reaction rates, due to the strong adsorption of the *CO intermediate on the Cu surface that promotes C-C bond formation via CO dimerization or CO-CHO coupling [5,12,15]. Unfortunately, the formation of C-C bonds on Cu is very complicated and the pathway remains elusive [16], which have greatly limited the development of highly selective electrocatalyst to reduce CO_2 to C_n ($n \geq 2$) liquid products.

Herein, we report a Sn-based tandem catalyst consisting of SnS_2 nanosheets that are able to produce formate intermediates and single Sn atoms anchored on a 3D carbon support via a local SnO3 cluster (Sn_1-O3G) that generate *OCO(OH) bicarbonate intermediates, followed by C-C coupling to electrochemically reduce CO_2 to ethanol. Based on this strategy, an ethanol selectivity of more than 70% was achieved over a wide potential range from − 0.6 to -1.1 V versus the reversible hydrogen electrode (RHE). This catalyst was found to maintain 97% of its initial activity after 100 hours of continuous reaction at a geometric current density as high as 17.8 $mA{\cdot}cm^{-2}$. The C-C bond formation mechanism on this newly-developed tandem catalyst was elucidated by combining isotope ($^{13}CO_2$ and $H^{13}COOH$) labelling experiments with extensive density functional theory (DFT) studies, providing a highly efficient

C-C coupling pathway for ethanol synthesis via the CO_2RR, with a low activation energy, high selectivity and good stability. These properties can be attributed to the dual active centers of Sn and O in Sn_1-O3G, which are able to adsorb *CHO and *CO(OH) intermediates, respectively, thereby promoting the subsequent C-C coupling of these intermediates to form ethanol. It is anticipated that this work will lead to new applications for single-atom catalysts [17,18] with polar active centers in multi-step chemical reactions.

The Sn-based tandem catalyst (denoted as SnS_2/Sn_1-O3G hereafter) was synthesized by a solvothermal method, the details of which are provided in the Extended data Figs. 21–22. We first evaluated the electrochemical CO_2RR performance of the SnS_2/Sn_1-O_3G using chronoamperometry in a H-type cell filled with CO_2-saturated 0.5 M $KHCO_3$ solution (Extended data Figs. 23–28). Extended data Fig. 25a provides typical current profiles obtained from the SnS_2/Sn_1-O3G, biased at various potentials from − 0.6 to -1.1 V vs. RHE in a CO_2-saturated 0.5 M $KHCO_3$ solution. The gaseous and liquid products were analyzed by an on-line gas chromatography and a nuclear magnetic resonance (NMR) spectroscopy (Extended data Figs. 1–20). The results obtained from combination of geometric current density of the potentiostatic electrolysis of CO_2 over SnS_2/Sn_1-O_3G and NMR spectral analysis (Extended data Figs. 8–13) are presented in Figs. 1a and b. These data show that the catalyst reproducibly yielded ethanol with a Faradaic efficiency (FE) as high as 82.5% at -0.9 V (vs. RHE) and a geometric current density of 17.8 mA/cm^2. More importantly, the FE associated with ethanol production was maintained above 70% over the potential window from − 0.6 to -1.1 V (vs. RHE). The yields of ethanol produced over SnS_2/Sn_1-O3G using isotopically labelled $^{13}CO_2$ and $^{12}CO_2$ at multiple points for different sampling intervals (2, 6 and 12 hours) are consistent quantitatively (Extended data Figs. 27, 28). This SnS_2/Sn_1-O3G catalyst was also extremely stable during CO_2 reduction to ethanol, maintaining approximately 80% ethanol selectivity at -0.9 V (vs. RHE) and 97% of its initial activity after 100 hours of continuous reaction (Fig. 1c). It is worth noting that no other C2 products (such as ethylene or acetate) were detectable over the entire potential range applied during the CO_2RR. Compared to state-of-the-art catalysts for electrochemical CO_2 reduction to ethanol (Fig. 1d), our Sn-based tandem catalyst shows the best CO_2-to-ethanol performance.

To study the superb CO_2RR performance to ethanol, the as-synthesized catalyst was carefully characterized by scanning electron microscopy (SEM), transmission electron microscopy (TEM), sub-angström-resolution high-angle annular dark-field scanning transmission electron microscopy (HAADF-STEM), X-ray diffraction (XRD), Raman spectroscopy, X-ray photoelectron spectroscopy (XPS) and X-ray absorption spectroscopy (XAS) to reveal the structural information. The SnS_2/Sn_1-O3G catalyst comprises of two components: vertically-aligned SnS_2 nanosheets (Extended data Figs. 29a) grown on a 3D carbon support decorated with atomically-dispersed Sn atoms (Figs. 2d and h). XPS and inductively coupled plasma mass spectrometry (ICP-MS) results show negligible metal contaminations (other than Sn) in 3D carbon and SnS_2/Sn_1-O3G (Extended data Figs. 30,31 and Table 7). To probe the exact local structure and coordination environment of these single Sn atoms on the carbon support, the SnS_2 nanosheets were removed by acid etching, as shown in Fig. 2c, confirmed by XPS and SEM analyses

(Extended data Figs. 33–34). Figure 2d presents a HAADF-STEM image of the acid-etched SnS_2/Sn_1-O3G (that is, the Sn_1-O3G) in which bright spots corresponding to metal atoms are clearly seen to be well dispersed across the carbon framework. Figure 2e provides enlarged images of the areas indicated in Fig. 2d and shows that each metal atom is connected to the carbon substrate via three bonds. The line profile in Extended data Fig. 35 demonstrates bright spots with sizes of approximately 0.2 nm while the electron energy loss spectroscopy (EELS) spectra as shown in Fig. 2f indicate that around 475 and 540 eV, corresponding to the Sn M edge and O K edge [19], the intensity from the bright spot is stronger than that from the dark area. The insert to Fig. 2d highlights the difference in the EELS spectra obtained from the two regions and confirms that bright spots in the HAADF-STEM image are Sn atoms, and that these atoms are in an oxygen-rich environment. The Sn content in Sn_1-O3G is 0.8 wt.% determined by ICP-MS.

The chemical oxidation state and coordination environment of the single Sn atoms were further examined by XAS. Figure 2g shows the Sn K edge X-ray absorption near edge structure (XANES) spectra of Sn_1-O3G and reference Sn foil (Sn^0), Sn (II) porphyrin (Sn^{2+}) and Sn (IV) porphyrin (Sn^{4+}). By comparing the energy positions of the white lines and the rising edges, the oxidation state of the Sn atoms in the Sn_1-O3G was determined to be + 4, in good agreement with the XPS and Mössbauer spectroscopy results (isomer shift and quadrupole splitting are 0.088 mm s^{-1} and 0.22 mm s^{-1}, respectively, Extended data Fig. 33d) [20]. Figure 2h shows the Fourier transform of the phase-uncorrected extended X-ray absorption fine structure (EXAFS) spectra. The peaks centered at 2.3 and 3.8 Å, corresponding to Sn-Sn interactions in Sn foil, are not present in the Sn_1-O3G spectrum, suggesting a high degree of dispersion of the Sn atoms in Sn_1-O3G, which is consistent with the HAADF-STEM results. The main peak in the Sn_1-O3G spectrum appears at approximately 1.60 Å, which is shorter than those associated with the Sn-N bonds in Sn (II) porphyrin and Sn (IV) porphyrin. The wavelet contour plot of the Sn_1-O3G (Fig. 2i) exhibits only one intensity maximum at approximately 5.2 $Å^{-1}$, which does not contain a peak that can be indexed to Sn-Sn coordination, as is evident in the wavelet contour plot for the Sn foil in Extended data Fig. 36. Considering that the 3D carbon support has a high concentration of oxygen functional groups (as demonstrated by the XPS and XAS results in Extended data Figs. 38 and 39) but does not contain N, this peak can be assigned to either Sn-O or Sn-C bond. The first shell of the Fourier transformation of the EXAFS spectrum of Sn_1-O3G was fitted with Sn-O or Sn-C back-scattering path (Extended data Fig. 40) and Extended data Table 6 summarizes the fitting results. A coordination number of approximately 3.7 was determined using Sn-O, but a value of 6.8 was obtained using Sn-C. Based on the low temperature synthesis employed and the HAADF-STEM as well as the EELS, XPS, XAS and Mössbauer spectroscopy results (Fig. 2d), the Sn atoms in Sn_1-O3G are deduced to coordinate to O atoms rather than C. The different charge densities and coordination environments of the Sn and O atoms render the Sn atoms electron-deficient and the surrounding O atoms electron-rich, and the spin-density population and Bader charge analysis implies a + 4 oxidation state for Sn (Extended data Fig. 41). Combining our experimental results with theoretical calculations, it appears that the Sn atoms in Sn_1-O3G were immobilized on the O-rich carbon support through binding with three O atoms to form a tridentate complex with an additional OH to stabilize the single Sn atoms, that is, Sn_1-O3(OH)G, as shown in the

insert to Fig. 2j. DFT calculation gives the formation energy of the Sn_1-O3(OH)G site of -4.75 eV, suggesting thermodynamically stable structure of Sn_1-O3(OH)G. Further XAS and HAADF-STEM investigations (Extended data Fig. 42) indicate that the O atoms coordinated Sn catalytic sites are robust in the CO_2RR process.

To understand the role of each component in the SnS_2/Sn_1-O3G for the CO_2RR, we synthesized SnS_2 nanosheets using the same protocol as for the SnS_2/Sn_1-O3G but without including a carbon support (structural information regarding the resulting SnS_2 is provided in Extended data Fig. 43). The SnS_2 nanosheets were found to catalyze electrochemical CO_2 reduction to give formate with an FE of approximately 60% at -0.9 V (vs. RHE) (Fig. 3a), in agreement with the previous report [21]. In contrast, Sn_1-O3G alone was only able to reduce CO_2 to CO as the main CO_2RR product (Fig. 3b). Interestingly, a mechanically-mixed combination of SnS_2 nanosheets and Sn_1-O3G was found to produce ethanol with an FE of approximately 15% at -0.9 V (vs. RHE) (Fig. 3c), while a mixture of SnS_2 nanosheets with 3D carbon (without the single Sn atoms, Extended data Fig. 44) failed to produce ethanol. From these findings, we propose that the formation of ethanol over the SnS_2/Sn_1-O3G may result from C-C coupling between the two intermediates associated with formate and CO.

To verify our hypothesis, we intentionally introduced a small amount of HCOOH into the reaction system (in a Na_2SO_4 electrolyte instead of $KHCO_3$) during the CO_2RR over the Sn_1-O3G. As shown in Fig. 3d, compared to the case without HCOOH (Fig. 3b), the cathodic current exhibits a clear decrease in the N_2-saturated Na_2SO_4 electrolyte upon HCOOH addition (Extended data Fig. 45). A similar trend was also observed in the CO_2-saturated electrolyte, suggesting that HCOOH affected the electrochemical reaction. In CO_2-saturated electrolyte, the FE_{CO} was found to decrease with increase in the amount of HCOOH, while the $FE_{ethanol}$ value increased. The inset in Fig. 3d summarizes the CO_2RR performance of Sn_1-O3G with addition of HCOOH in a CO_2-saturated Na_2SO_4 electrolyte at various applied potentials. At an applied potential of -1.0 V (vs. RHE), adding HCOOH (50 μL) to the CO_2-saturated electrolyte decreased the FE_{CO} (inset in Fig. 3b) from 50% to approximately 40%, while increasing $FE_{ethanol}$ nearly 40-fold, from close to 0.2–7.4%. The partial geometric current density associated with ethanol formation also increased, from 0.002 to 0.9 mA/cm^2. These results demonstrate the importance of HCOOH in C-C coupling to form ethanol on O atoms coordinated Sn catalytic sites. In contrast, unlike the result for the Sn_1-O3G catalyst, the Sn_1-N4G catalyst (with 4 nitrogen atoms coordinated Sn center) failed to produce any C2 products in CO_2RR with addition of HCOOH (Extended data Figs. 46 and 47), indicating the critical roles of both the single atomic Sn center and the coordinated oxygen atoms in Sn_1-O3G for the C-C coupling reaction. We also investigated the CO_2RR products generated by the Sn_1-O3G catalyst using gaseous CO and HCOOH as the reactants and found no C2 products, indicating the critical role of the adsorbed *CO(OH) intermediate (see below) formed via CO_2 reduction on the Sn_1-O3G site in the formation of ethanol.

To elucidate the mechanism of ethanol formation through the CO_2RR, isotopically-labeled reactants ($^{12}CO_2$, $^{13}CO_2$, H^{12}COOH and H^{13}COOH) were used to trace the pathway of the C atoms in the final C2 product formed on the Sn_1-O3G catalyst. Figure 3e and Extended data Fig. 48 show that the methyl C (*CH_3) in ethanol comes from HCOOH, while the C in CO_2 goes to the methylene C (*CH_2OH). Therefore, Fig. 3f schematically summarizes the CO_2RR process to form ethanol taking place on the SnS_2/Sn_1-O3G. The comprehensive discussion for the ethanol formation process on the SnS_2/Sn_1-O3G tandem catalyst is provided from additional structural characterization and kinetics simulation (Extended data Figs. 49–53 and Tables 9–17), indicating that diffusion of HCOOH generated from the SnS_2 component to the single atomic Sn sites on Sn_1-O3G is the rate-determining step for ethanol formation.

Based on the above experimental results, we built the active site model of the catalyst. Extensive DFT calculations were performed using the computational hydrogen electrode (CHE) model [22,23,24,25] to map the CO_2RR pathway and energetics during the formation of ethanol. The results show that, during the CO_2 reduction process, the proton-coupled electron transfer (PCET, H^+/e^-) and dehydration of the Sn_1-O3(OH)G pre-catalytic sites is exergonic and the resulting Sn_1-O3G is of radical nature (going from species **0** to **1** in Fig. 4, Extended data Figs. 54 and 55). Two possible CO_2 binding mechanisms were assessed: monodentate (**2 – 1**) and side-on (**2**) [26,27] (Extended data Fig. 56a). Thus, there are two possible pathways for CO_2 reduction, one of which produces CO and the other produces ethanol. Free energy pathways for competing C1 and C2 products were systematically calculated as shown in Extended data Figs. 56–57 and Extended data Table 18. In the case of species **2**, the O2SnO…C linkage is cleaved and a face-to-face cyclo-addition between Sn = O double bond and O = CO double bond leads to the CO_2 activation, with a CO_2 adsorption free energy of -0.75 eV. The activated *$\mathbf{CO_2}$ (marked in bold) can then have a PCET to form O2Sn-O-**CO**(**O**H) in **3**, with exergonicity of 1.68 eV. This bicarbonate species *O**CO**(**O**H) is formed as the dominant intermediate in the hydrogenation process of *$\mathbf{CO_2}$ catalyzed by O2Sn = O. As a result of forming the strongly bound carbonate species, it hardly generates CO directly except from the recovered catalyst via **3 – 1** intermediate (as shown in Extended data Fig. 55b). The differential charge distribution analysis and Bader charges of **3** determined that the positive charge was higher on the Sn atom, such that bonding between Sn atom and HCOOH (externally added or *in-situ* produced over SnS_2) was favored. With PCET, the carbonyl group in HCOOH* can easily dehydrate to generate Sn-CHO in intermediate **4**, with a free energy barrier of 0.52 eV. This intermediate **4** features *CHO on Sn and *CO(OH) on the neighboring O (i.e., O2Sn-O-CO(OH) bicarbonate), which explains the activities of Sn and O atoms as the dual active centers in the Sn_1-O3G. Following the drastic reduction of all carbonyl groups in **4**, intermediate **5** is formed as the precursor for C-C coupling. The free energy barrier to C-C bond formation is 0.13 eV, which is much lower than those of Cu-based catalysts (> 1.0 eV) [13,28]. Thus, intermediate **6**, which contains a Sn-C-**C-O** quaternary ring, is obtained. As reduction proceeds, with exergonicity of 0.99 eV, the Sn-C bond breaks upon further PCET, then forms the *CH_3**C**H**O**H intermediate (**7**), followed by PCET and O-C bond cleavage (with a free energy barrier of 0.87 eV), and finally releases CH_3CH_2OH from the active site. Owing to the flexibility of the bond between the active O

atom of Sn_1-O3 and the C of the support, the Sn_1-O3G catalyst is distinguished by the dual active sites of Sn and O that are able to adsorb different C-based intermediates, providing a novel platform for C-C bond formation during the CO_2RR to produce ethanol.

In summary, we have developed a Cu-free, Sn-based tandem catalyst to produce ethanol from the CO_2RR, in which the dual active centers of Sn and O atoms on Sn_1-O3G serve to adsorb different C-based intermediates, which effectively lowers the C-C coupling energy between *CO(OH) and *CHO. Our tandem catalyst enables a *formal-bicarbonate* coupling pathway, which not only provides a novel platform for C-C bond formation during ethanol synthesis and overcomes the restrictions of Cu-based catalysts, but also offers a unique strategy for manipulating CO_2 reduction pathways toward desired products.

References

1. Hasselmann, K. *et al.* The challenge of long-term climate change. *Science* **302**, 1923-1925 (2003).
2. Meinshausen, M. *et al.* Greenhouse-gas emission targets for limiting global warming to 2 degrees C. *Nature* **458**, 1158-1162 (2009).
3. Mehling, M. A., Metcalf, G. E. & Stavins R. N. Linking Climate Policies to Advance Global Mitigation. *Science* **359**, 997-998 (2018).
4. Li, C. W., Ciston, J. & Kanan, M. W. Electroreduction of Carbon Monoxide to Liquid Fuel on Oxide-Derived Nanocrystalline Copper. *Nature* **508**, 504 (2014).
5. Zhuang, T.-T. *et al.* Steering post-C-C coupling selectivity enables high efficiency electroreduction of carbon dioxide to multi-carbon alcohols. *Nat. Catal.* **1**, 421-428 (2018).
6. Zhuang, T.-T. *et al.* Copper nanocavities confine intermediates for efficient electrosynthesis of C3 alcohol fuels from carbon monoxide. *Nat. Catal.* **1**, 946-951 (2018).
7. Huang, Y. *et al.* Elucidating the electrocatalytic CO_2 reduction reaction over a model single-atom nickel catalyst. *Angew. Chem. Int. Ed.* **58**, 2-8 (2019).
8. Yang, H. B. *et al.* Atomically dispersed Ni(i) as the active site for electrochemical CO_2 reduction. *Nat. Energy* **3**, 140-147 (2018).
9. Shih, C. F., Zhang, T., Li, J. & Bai, C. Powering the future with liquid sunshine. *Joule* **2**, 1925-1949 (2018).
10. Farrell, A. E. *et al.* Ethanol can contribute to energy and environmental goals. *Science* **311**, 506-508 (2006).
11. Spurgeon, J. M. & Kumar, B. A comparative technoeconomic analysis of pathways for commercial electrochemical CO_2 reduction to liquid products. *Energy Environ. Sci.* **11**, 1536-1551 (2018).
12. Peterson, A. A., Abild-Pedersen, F., Studt, F., Rossmeisl, J. & Nørskov, J. K. How copper catalyzes the electroreduction of carbon dioxide into hydrocarbon fuels. *Energy Environ. Sci.* **3**, 1311-1315 (2010).
13. Calle-Vallejo, F. & Koper, M. T. M. Theoretical considerations on the electroreduction of CO to C_2 species on Cu (100) electrodes. *Angew. Chem. Int. Ed.* **125**, 7423-7426 (2013).

14. Garza, A. J., Bell, A. T. & Head-Gordon, M. Mechanism of CO_2 reduction at copper surfaces: pathways to C_2 products. *ACS Catal.* **8**, 1490-1499 (2018).
15. Montoya, J. H., Peterson, A. A. & Nørskov, J. K. Insights into C–C coupling in CO2 electroreduction on copper electrodes. *ChemCatChem* **5**, 737-742 (2013).
16. Nitopi S. *et al.* Progress and perspectives of electrochemical CO_2 reduction on copper in aqueous electrolyte. *Chem. Rev.* **119**, 7610-7672 (2019).
17. Qiao B. *et al.* Single-atom catalysis of CO oxidation using Pt_1/FeO_x. *Nat. Chem.* **3**, 634-641 (2011).
18. Wang A., Li, J. & Zhang T. Heterogeneous single-atom catalysis. *Nat. Rev. Chem.* **2**, 65-81 (2018).
19. de la Peña F. *et al.* Mapping titanium and tin oxide phases using EELS: an application of independent component analysis. *Ultramicroscopy* **111**, 169-176 (2011).
20. Hiroyuki H. *et al.* Discovery of a novel Sn(II)-based oxide β-$SnMoO_4$ for daylight-driven photocatalysis. *Adv. Sci.* **4**, 1600246-1600253 (2017).
21. Zheng X. *et al.* Sulfur-modulated tin sites enable highly selective electrochemical reduction of CO_2 to formate. *Joule* **1**, 794-805 (2017).
22. Kresse G. & Furthmüller, J. Efficiency of *ab-initio* total energy calculations for metals and semiconductors using a plane-wave basis set. *Comp. Materials Science* **6**, 15-50 (1996).
23. Kresse, G. & Furthmüller, J. Efficient iterative schemes for *ab-initio* total-energy calculations using a plane-wave basis set. *Phys. Rev. B* **54**, 11169-11186 (1996).
24. Nørskov J. K. *et al.* Origin of the overpotential for oxygen reduction at a fuel-cell cathode. *J. Phys. Chem. B* **108**, 17886-17892 (2004).
25. Rossmeisl, J. Z., Qu, W., Zhu, H., Kroes, G. J. & Nørskov, J. K. Electrolysis of water on oxide surfaces. *J. Electroanal. Chem.* **607**, 83-89 (2007).
26. Taifan, W., Boily, J.-F. & Baltrusaitis J. Surface chemistry of carbon dioxide revisited. *Surf. Sci. Rep.* **71**, 595-671 (2016).
27. Freund, H. J. & Roberts, M. W. Surface chemistry of carbon dioxide. *Surf. Sci. Rep.* **25**, 225-273 (1996).
28. Luo, W. Nie, X. Janik, M. J. & Asthagiri, A. Facet dependence of CO_2 reduction paths on Cu electrodes. *ACS Catal.* **6**, 219-229 (2016).

Declarations

Acknowledgments

The authors thank Y.L., X.L., L.K., Y.R. and J.Y. for XAS support, and X.P. for high-resolution TEM measurements. The authors also thank the BL14W at the Shanghai Synchrotron Radiation Facility and BL-20A at the National Synchrotron Radiation Research Center (Hsinchu, Taiwan) for the XAS experiments.

Funding: This work was supported by the Strategic Priority Research Program of the Chinese Academy of Sciences (XDB36030200), CAS Project for Young Scientists in Basic Research (YSBR-022), the National Natural Science Foundation of China (22033005, 21776269, U19A2015, 21902182, 22075195, 21925803 and 22179016), Jiangsu Specially-Appointed Professor Program, the Fundamental Research Funds for the Central Universities (2022YQHH01), the Guangdong Provincial Key Laboratory of Catalysis (No. 2020B121201002), and the Singapore Ministry of Education Academic Research Fund (AcRF) Tier 1: RG4/20, RG2/21 and Tier 2: MOET2EP10120-0002.

Author contributions: J.D., H.Y., Y.H., T.Z. and B.L. conceived and designed the project. J.D. conducted materials synthesis and electrochemical measurements. J.D. and S.L. built the NMR analysis methods. W.L. performed the HADDF-STEM measurement. X.M. and J.L. carried out the DFT modeling and analyzed the mechanism. Q.M. performed the kinetics simulation. J.D., H.Y. and B.L. analyzed the experimental data and wrote the paper with the help from all authors.

Data and materials availability: All data are reported in the main text and Extended data.

Figures

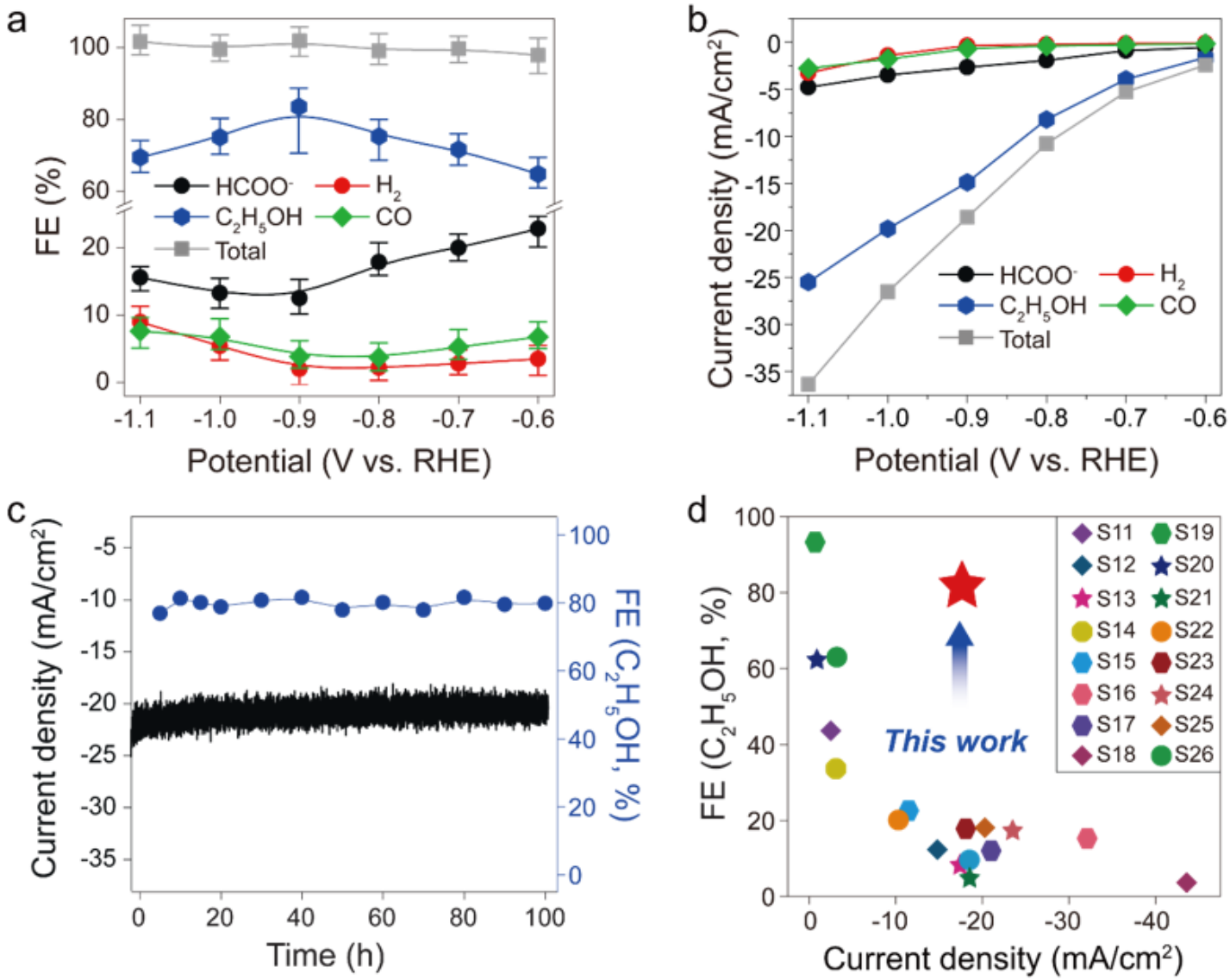

Figure 1

The CO_2RR performance of the SnS_2/ Sn_1-O3G tandem catalyst. (**a**) FE values with error bars indicated (the FE was measured in 2 h interval at each potential), (**b**) partial current density and total current density, (**c**) stability test performed at -0.9 V (vs. RHE), and (**d**) comparison of the CO_2RR performance to ethanol in aqueous system. Detailed data are provided in Extended data Table 6. Catalyst loading: 0.5 mg/cm^2. All measurements were performed at 1 atm CO_2 and room temperature in 0.5 M $KHCO_3$ (pH = 7.3). Error bars represent the standard deviation of 3 replicate measurements.

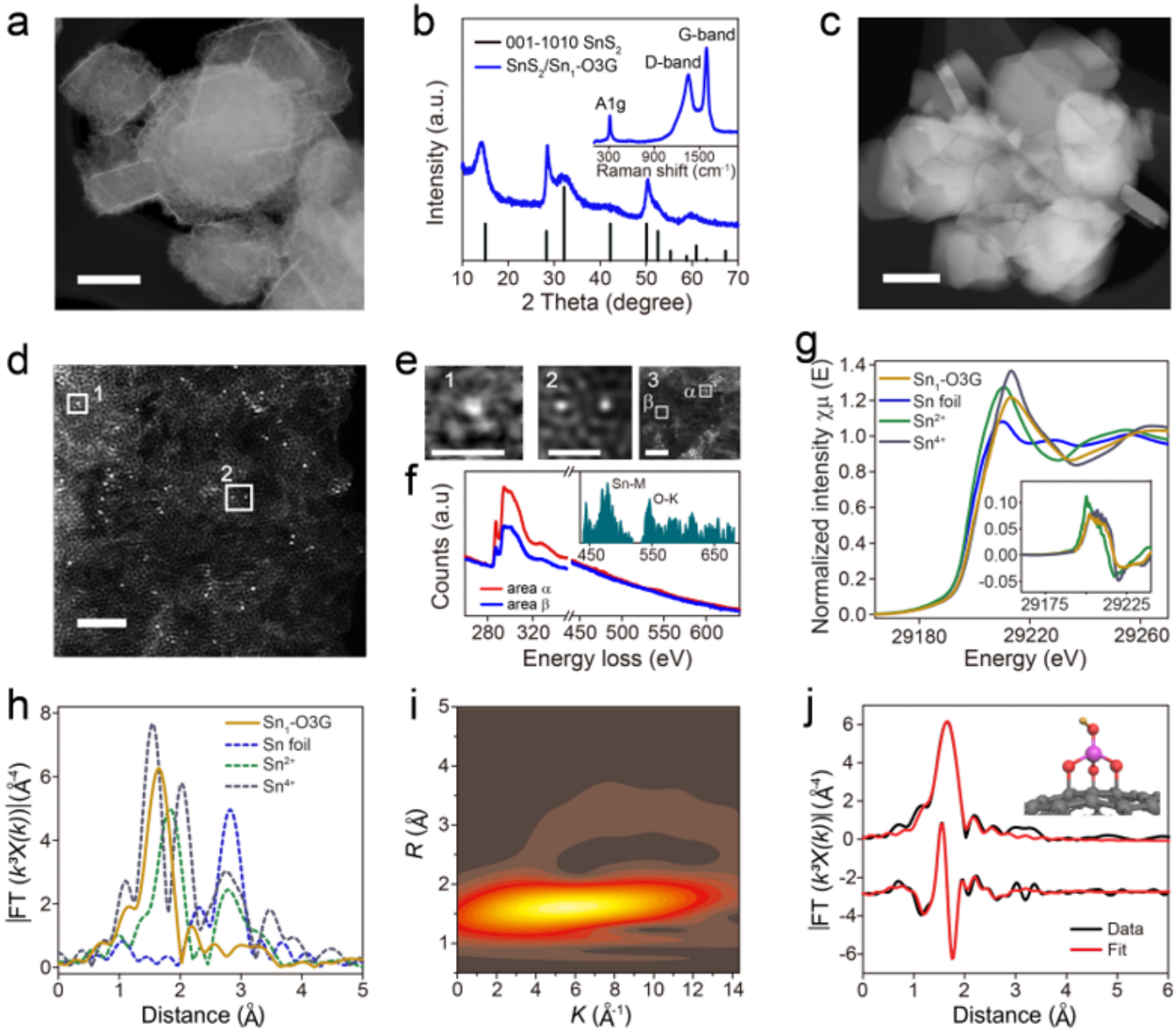

Figure 2

Structural characterizations of SnS_2/Sn_1-O3G and Sn_1-O3G. (**a**) A STEM image and (**b**) XRD pattern of the SnS_2/Sn_1-O3G, with the Raman spectrum provided in the inset, (**c**) a STEM image of the Sn_1-O3G (after SnS_2 was removed by acid etching), (**d**) a HAADF-STEM image showing the distribution of single Sn atoms on the carbon matrix, (**e**) expanded views of (**d**), revealing the atomic configuration of Sn (scale bars: 2 and 0.5 nm in areas 1 and 2), (**f**) EELS spectra obtained from the two sites indicated in **e**(3) (scale bar: 2 nm), with the difference between the two spectra (in the range from 440 to 700 eV) highlighted in the inset, (**g**) Sn K-edge XANES spectra, with an insert showing the first derivative of the Sn K edge for Sn_1-O3G, Sn (II) porphyrin and Sn (IV) porphyrin, (**h**) Fourier-transformed (phase uncorrected) Sn K-edge EXAFS spectra, (**i**) the wavelet transform of the *k3*-weighted EXAFS spectrum of the Sn_1-O3G (data for SnS_2/Sn_1-O3G, Sn^{2+} and Sn^{4+} are shown in Extended data Fig. 36; *k3*-weighted k-space spectra are

shown in Extended data Fig. 37), and (**j**) first-shell fitting of the Fourier transformation of the EXAFS spectrum of Sn_1-O3G (the EXAFS spectrum was fitted using the FEFF 8.2 code, and the inset shows an atomic model for Sn_1-O3G where grey, red, yellow and purple spheres represent C, O, H and Sn atoms, respectively).

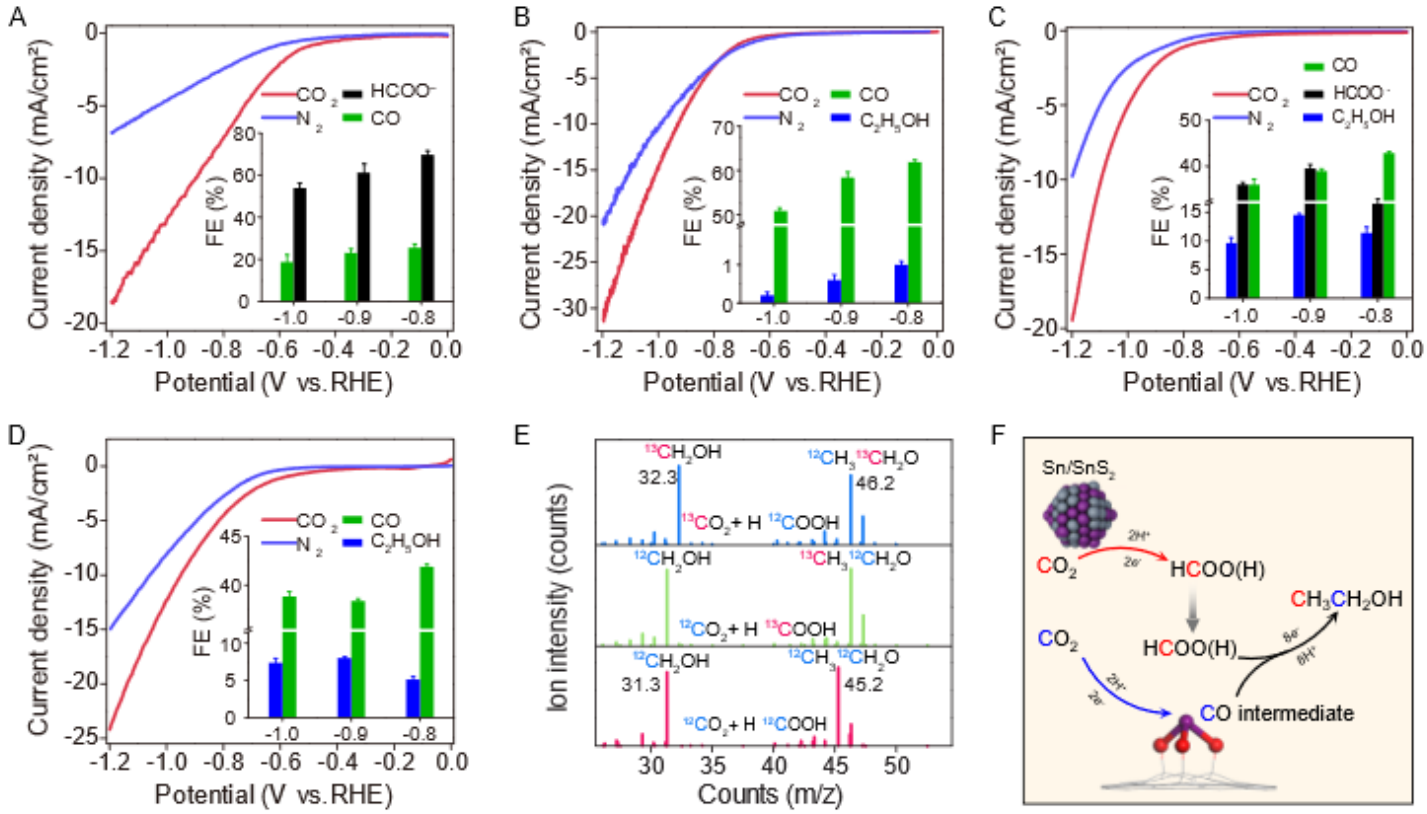

Figure 3

CO_2 reduction to ethanol. (**a**) and (**b**) LSV curves of SnS_2 nanosheets and Sn_1-O3G. Inset displays the FE, (**c**) LSV curves and FE data for a physical mixture of SnS_2 and Sn_1-O3G with a 1:1 mass ratio, (**d**) LSV curves and FE data for Sn_1-O3G with HCOOH addition (see Extended data Fig. 43 for the CO_2RR characteristics of the 3D carbon electrode), (**e**) mass spectra of the CO_2 reduction products using $^{13}CO_2$ (top) or H^{13}COOH (middle) as the reactant, biased at -0.9 V vs. RHE, or using $^{12}CO_2$ and H^{12}COOH (bottom) as the reactants under the same electrochemical conditions, and (**f**) a schematic illustration showing the cascade reaction during CO_2 reduction to ethanol over SnS_2/Sn_1-O3G (grey: S, red: O, yellow: H and purple: Sn). Catalyst loading: 0.5 mg/cm^2. All measurements were performed at 1 atm CO_2 and room temperature in 0.5 M $KHCO_3$ (pH = 7.3). Error bars represent the standard deviation of 3 replicate measurements.

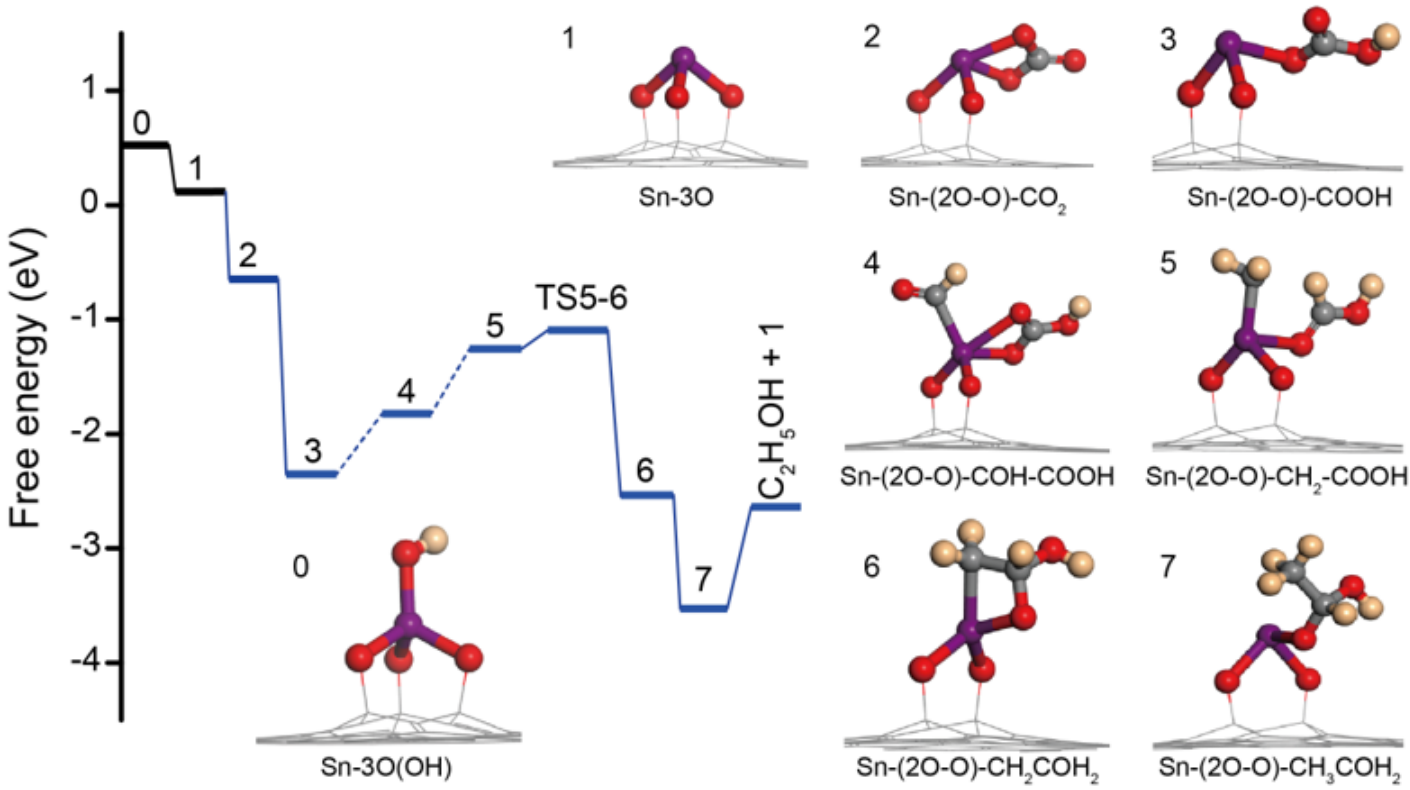

Figure 4

C-C bond formation via a *formyl-bicarbonate* coupling pathway (with a key intermediate 4). Reaction energy profiles and the corresponding intermediate structures (**0** to **7**) for the formation of ethanol via the CO_2RR on the Sn_1-O3G catalyst. Extended data Fig. 58 shows the detailed free energy profiles for **3** to **5**.

Supplementary Files

This is a list of supplementary files associated with this preprint. Click to download.

- ExtendedData.docx